Available online at www.sciencedirect.com
ScienceDirect
Magnetic Resonance Imaging 28 (2010) 1497–1506
MAGNETIC RESONANCE IMAGING

Diffusion tensor image up-sampling: a registration-based approach

Zhenhua Mai[a,*], Marleen Verhoye[b], Annemie Van der Linden[b], Jan Sijbers[a]

[a]IBBT-VisionLab, Department of Physics, Universiteit Antwerpen, Antwerpen, Wilrijk, 2610, Belgium
[b]Bio-Imaging Lab, Biomedical Department, Universiteit Antwerpen, Antwerpen, Belgium

Received 30 September 2009; revised 19 April 2010; accepted 25 June 2010

Abstract

Diffusion weighted images (DWI), from which the corresponding diffusion tensor images (DTI) are estimated, are commonly acquired with anisotropic discretizations. Traditional methods to up-sample diffusion weighted images generally rely on scene-based interpolation and do not exploit structural information from the images. In this study, a DTI up-sampling framework is presented that incorporates the underlying anatomical shape information by means of non-rigid inter-slice registration. A strategy is proposed to reorient the interpolated tensor in order to maintain its proper orientation. Tests on phantom as well as on real data sets show that the proposed method is able to produce better results compared to scene based interpolation methods in terms of the accuracy of DWI/DTI interpolation, especially when diffusion tensor orientation is taken into account.

Keywords: DWI/DTI; Up-sampling; Registration-based

1. Introduction

In typical medical imaging systems, the acquired images are usually organized in a slice by slice fashion. The distance between consecutive slices is generally larger than that between two neighboring voxels in the same slice, which results in anisotropic discrete grids. However, many image processing tasks, such as visualization, manipulation, and analysis of image data [1] often require isotropically sampled volume data. Hence, there is a need for techniques that up-sample anisotropic image into an isotropic discretization.

In general, interpolation methods can be grouped into two categories [2]:

Scene-based interpolation

In scene-based methods, the interpolated (INT) image intensities are mostly determined by their spatial relation to existing intensities. Linear, cubic spline and window sinc interpolations [3,4] are the typical variants among them. Despite their relatively easy implementation and high speed, this group of methods can produce many interpolation errors (see Fig. 1).

Object-based interpolation

In object-based methods, the INT intensities are determined by extracting and incorporating information about the imaged objects, features or structures inherent in the image. Methods for information extraction include contour extraction, correspondence registration, etc. Our framework roughly follows the concept proposed by Goshtasby et al. in [5]: neighboring slices are registered, after which the transformation is used to guide the interpolation.

In comparison, object-based methods proved to be more accurate, mainly because the underlying image structures are accounted for.

In the literature, the up-sampling methods for conventional scalar images, such as ordinary magnetic resonance (MR) images, either based on scene-based method or object-based method, are well documented. However, for the target of this paper, the multi-valued diffusion weighted/tensor images, traditional treatments are mostly a direct extension of the scalar method to a vectorized one, for example, as done in the popular image processing toolset ITK [6]. More sophisticated methods have been proposed, for example, Tschumperle et al. [7] developed a vectorized anisotropic diffusion filter based on second-order Partial Differential Equation to address the problem of multi-valued image

* Corresponding author. Tel.: +32 32652442.
E-mail address: zhenhua.mai@ua.ac.be (Z. Mai).

0730-725X/$ – see front matter © 2010 Elsevier Inc. All rights reserved.
doi:10.1016/j.mri.2010.06.018

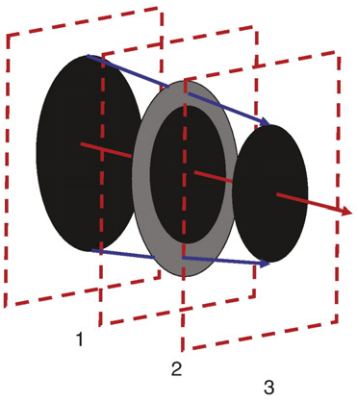

Fig. 1. A typical artifact generated by linear interpolation. The middle slice is interpolated linearly between the first and the third. Instead of showing the properly shrunken sphere, linear interpolation shows the gray shading.

interpolation. However, the anisotropic diffusion in the slicing direction will be heavily impeded by the partial volume effect inherent in the thick-sliced images, not to mention that their vectorization does not really take into account the specifics of the tensor geometry, such as tensor orientation.

In order to apply the aforementioned registration-based concept to the diffusion-weighted images (DWI)/diffusion tensor images (DTI) interpolation, with the proper appreciation for the tensor information, it is imperative to consider the progresses made regarding DWI/DTI registration. Alexander et al. adapted the multi-resolution elastic matching algorithm [8] for matching DTI, and also proposed different strategies for tensor reorientation (TR). Unfortunately, their method does not incorporate a free-form registration method, resulting in a limited degree of freedom in the produced transform and the limited quality of registration. Rohde et al. [9] proposed an intensity based registration method capable of performing affine and nonlinear registration of multichannel images. A more sophisticated non-rigid registration based on a viscous fluid model was proposed by Van Hecke et al. [10], with excellent results. In order to maximize the registration correspondence, Studholme [11] proposed a multi-channel (MC) mutual information (MI) metric, with inter-channel interaction, to include the DT information into the optimization to achieve a better registration. It is clear that not only a free-form non-rigid registration is needed, but also is necessary a maximized information combination involving both DW and DTI. Furthermore, with respect to tensor reorientation, Chao et al. have investigated the influence of different interpolation methods on the regional fractional anisotropic study after spatial normalization [12]. The importance of tensor reorientation in the interpolation context will also be addressed in this paper.

Recently, a Riemannian framework based on an advanced handling of DTI tensors in their mathematically native Riemannian space was proposed by Pennec et al. [13]. Not only does it provide a new method for a direct DTI interpolation (without interpolating first on DWI), but also does it eliminate some of the less desirable effects of the traditional Euclidean tensor interpolation.

In view of the variety of DW/DT registration methods, we developed our interpolation framework as follows:

1. Non-rigid DWI/DTI inter-slice registration is performed in order to obtain the displacements that morph image features between neighboring slices.
2. Proper intermediate displacements are determined to warp the image onto the interpolation plane, after which the corresponding INT DT is reoriented.

Our method starts by interpolation of the DWI, followed by DTI estimation. We will group methods operating in similar manner as DWDT interpolation, as opposed to another method group that directly interpolates on tensors, which will be referred to as Direct Diffusion Tensor (DiDT) interpolation. The common methods in the DWDT group include the linear interpolation and the windowed sinc interpolation, while the DiDT group includes the traditional tensor matrix coefficient interpolation (which will be later denoted as Euclidean interpolation) and the newly emerged Riemannian interpolation. In this paper, we also compare both method groups.

This paper will be organized as follows: Section 2 details the methodology for both registration and interpolation, including tensor reorientation. Section 3 discusses results obtained from both phantom and real data tests. Finally, in Section 4, we will give some concluding remarks as well as some prospect for future work.

2. Method

As mentioned in the introduction, our method mainly consists of two parts: the first part is a non-rigid inter-slice registration to determine the inter-slice feature correspondence, and the second part is an adaptive interpolation guided by the correspondence.

2.1. Registration framework

The common objective in two-dimensional image registration is to achieve spatial correspondence between two images: the target, or end image $E=E(x,y)$ with spatial coordinates (x,y), and the source, or start image $S=S(x',y')$ with spatial coordinates (x',y'). Both images are defined on the same 2D domain, or (x,y), $(x',y')\in\Omega=\{(i,j)|0\le i<X, 0\le j<Y\}$, where X and Y denote the dimensions of the image. The correspondence is a function that maps (x,y) to (x',y'), $f(x,y)\rightarrow(x',y')$. A mapping can be either parametric or non-parametric. A parametric mapping is typically associated with rigid spatial transformations, e.g., translation, rotation, scaling, etc., that are parameterized by global parameters, such as translational displacement, rotation angle and scaling factor. A non-parametric mapping is

typically associated with non-rigid spatial transformations and does not have a closed form expression as a function of global parameters. Both types of mappings can be written as

$$f(x',y') = (x,y) + \vec{d}(x,y) \tag{1}$$

where $\vec{d}(x,y)$ denotes the displacement vector.

For two images to be registered, the correspondence should maximize a similarity measure, wherein we have the optimum displacement field:

$$\vec{d}^{m}(x,y) = \arg\min_{\vec{d}(x,y)} \mathscr{E}\left\{S\left[(x,y) + \vec{d}(x,y)\right], E(x,y)\right\} \tag{2}$$

where $\mathscr{E}[.]$ is a cost energy function (CEF) that evaluates how good a certain mapping f is in achieving the correspondence between two images. The specific form for the actual CEF will be given in the following sections.

As discussed in the introduction, DTI/DWI registration techniques based on different similarity measures come in great variety. For our task, two registration models, Optical flow registration and MI registration, prove to be favorable, because they are able to achieve accurate registration in an efficient way. This is preferable, given the fact that image interpolation serves mainly as an intermediate step between image acquisition and image analysis.

2.1.1. Optical flow registration

Optical flow is the pattern of apparent motion associated with objects in a visual scene [14]. It is widely used in image/video processing such as motion detection and motion compensated encoding. The relevancy of the optical flow method to inter-slice interpolation is obvious: the spatial transformation between consecutive slices can be viewed as temporal morphology of the anatomical features that can be captured by the optical flow.

The optical flow constraint equation has different variants [14]. Here we use the force-symmetric optical flow constraint equation:

$$\frac{1}{2}\vec{d}(x,y)\cdot\left[\vec{\nabla}I_s(x,y) + \vec{\nabla}I_e(x,y)\right] = (I_s - I_e). \tag{3}$$

where $\vec{d}(x,y)$ is the displacement vector, and $\vec{\nabla}I_s(x,y)$ and $\vec{\nabla}I_e(x,y)$ are the spatial gradients of the intensity at (x,y) of the starting and the end slice, respectively. Instead of solving, Eq. (3) directly, we construct a cost energy function $\mathscr{E}[\vec{d}]$ that, after minimization, leads to the optimal displacement field $\vec{d}(x,y)$:

$$\mathscr{E}\left[\vec{d}\right] = \iint_{\Omega} dxdy\left\{\frac{1}{2}\vec{d}\left[\vec{\nabla}I_s(x,y) + \vec{\nabla}I_e(x,y)\right] - (I_s - I_e)\right\}^2 \tag{4}$$

The Controlled Grid (CG) technique [15] is used to search for the optimal $\vec{d}(x,y)$. In CG, the image slice is divided into a grid with uniform-sized cells g_k, with $n_x \times n_y$ control points $\phi_{i,j}$. Only the displacement vectors at the control points, $d_\phi(i,j)$, are free variables; the remaining vectors are interpolated with third order B-splines,

$$\vec{d}(x,y) = BS\left(d_\phi\right) = \sum_{l=0}^{3}\sum_{m=0}^{3} \mathrm{B_l(u)B_m(v)}d_\phi(i+l, j+m) \tag{5}$$

where d_ϕ denotes the set of control point displacement vectors, BS is the B-spline interpolation kernel, $i=[x/n_x]-1$, $j=[y/n_y]-1$, $u=x/n_x-[x/n_x]$, $v=y/n_y-[y/n_y]$, and B_l represents the lth basis function of the B-spline [16]. The purpose of using B-spline is also to accommodate a non-rigid free-form interslice transformation, as opposed to a rigid transformation that does not allow too many degrees of freedom.

It is obvious that the number of control points $n_x \times n_y$ determines the number of degrees of freedom in a mapping f. However, from the perspective of computational complexity, a bigger grid size leads to an exponentially bigger computational load. The proper procedure is to combine the benefits of low computational load and high degrees of freedom in a multi-resolutional approach [16]. That is, with grids of decreasing grid cell sizes, we can proceed hierarchically through a series of solutions to approximate the ideal one progressively. Let $\Phi^1,\ldots,\Phi^R$ denote a hierarchy of control grids with increasing grid sizes. Furthermore, each control grid Φ^r along with the associated B-spline interpolation defines a local deformation field $\vec{d^r}(x,y)$ at each level r. Their sum through the hierarchy forms the overall local deformation field:

$$\vec{d}(x,y) = \sum_{r=1}^{R} \vec{d^r}(x,y) \tag{6}$$

We assume that the number of control points in both x and y directions always doubles from one level r to the next level $r+1$. Therefore, the position of the control point $\phi_{2i,2j}^{r+1}$ is incident on that of the control point $\phi_{i,j}^{r}$. The displacement vectors for the new control points at level $r+1$ can be calculated from the values at level r using a B-spline decomposition algorithm [17]. Note that Eq. (4) is an analytical function of $\vec{d}(x,y)$, which in turn is a function of the grid control point displacement vectors $\vec{d}_\phi(i,j)$.

$$\mathscr{E}\left[d_\phi\right] = \iint_{\Omega} dxdy\left\{\frac{1}{2}BS\left(\vec{d}_\phi\right)\cdot\left[\vec{\nabla}I_s(x,y) + \vec{\nabla}I_e(x,y)\right] - (I_s - I_e)\right\}^2 \tag{7}$$

Hence, the gradient of Eq. (7) with respect to $\vec{d}_\phi(i,j)$ can be computed and used in a gradient descent search algorithm to speed up the optimization process.

2.1.2. MI registration

The structure of our MI registration resembles that of the optical flow registration, as we also use the CG technique to

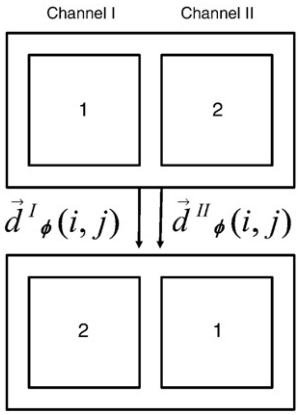

Fig. 2. The balanced bi-mapping registration mechanism. In Channel I, slice 1 is registered to slice 2, while in Channel II, slice 2 is registered to slice 1. The displacement parameters $\vec{d}^{I}_{\phi}(i,j)$ *and* $\vec{d}^{II}_{\phi}(i,j)$ are inverse to each other.

robustly minimize a *CEF* in order to find the optimal displacement field. However, we used MI to determine how optimal one displacement field is in matching two slices. In addition to its wide use in normal MR image registration, MI has also been proposed as a robust criterion for DTI similarity [10,18], even when the relation between the image intensities is not readily comparable. The MI between a start image deformed by a displacement field $\vec{d}_{\phi}(x,y)$, $S'=S[(x,y)+\vec{d}(x,y)]$, and an end image $E=E(x,y)$ can be expressed as

$$MI\left(\vec{d}(x,y)\right) = \sum_{I_s\in S'}\sum_{I_e\in E} p(I_s,I_e)\log\frac{p(I_s,I_e)}{p^{E}(I_e)p^{S'}I_s} \tag{8}$$

where I_s and I_e represent the intensities of images S' and E, $p(I_s,I_e)$ is the joint intensity distribution of the deformed start image and the end image, $p^{S'}(I_s)$ and $p^{E}(I_e)$ are the marginal intensity distribution of S' and E, respectively. Therefore, the CEF for MI registration with CG technique will take the following form:

$$\mathscr{E}\left[\vec{d}_{\phi}\right] = MI\left[BS\left(\vec{d}_{\phi}\right)\right], \tag{9}$$

where $\vec{d}_{\phi}$ is the set of control point displacement vectors, and *BS* is the same B-spline kernel as in the previous section. Since Eq. (9) is in closed analytical form, its gradient with respect to a specific $\vec{d}_{\phi}(i,j)$ can be computed analytically

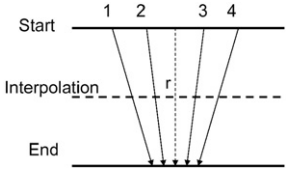

Fig. 3. An example illustrating the necessity for displacement vector interpolation. The four vectors 1–4 represent the displacements from the start slice to the end slice in this local area. For interpolating the intensity in point *r*, it is apparent that neither Vector 2 nor 3 is the proper choice, but their interpolation (dash line) is.

Table 1
A comparison of DWI interpolation methods with regards to MSE of INT DWI on phantom and real images with both B_0 image and an average over all DWI

MSE	Phantom		Real image	
	B_0 image	DWI avg.	B_0 image	DWI avg.
LI	69787	3503	10125	2796
wSinc	65.29%	71.05%	87.12%	96.10%
OF	57.01%	55.87%	74.92%	81.15%
ADW	55.75%	54.84%	73.05%	77.75%
DT	61.60%	62.75%	74.55%	86.70%
DWDT	54.81%	53.07%	73.36%	80.15%

Only the actual MSE for LI is shown here, the rest of the entries for other methods in the table are the ratios of their MSE to LI MSE. The ratio is computed as $MSE^{X}/MSE^{LI}\times 100\%$, where *X* stands for one of the methods listed in the table except LI.

and used in a gradient descent optimizer. In order to reach an optimal solution robustly, the CG technique is also used in a multi-resolutional manner.

2.1.3. Multi-channel registration

Practically, a registration procedure that is only based on DWIs is sufficient to extract the necessary information for interpolation. However, the incorporation of DT information into the registration can enhance it [19], especially in the white matter regions which, in general, are relatively homogeneous in the scalar-valued T_2-weighted images [11]. Therefore, we adopted our MI registration framework with an MC approach. That is, we can compute the MCMI for two multi-channel image, $S=\{S_i(x',y')|i=1,\ldots,N\}$ and $E=\{E_j(x,y)|j=1,\ldots,N\}$, where N is the number of image channels, and each $S_i(x',y')$ or $E_j(x,y)$ is defined on the same 2D domain Ω as the single-channel image. The MCMI is computed as

$$MCMI\left(\vec{d}(x,y)\right) = \sum_{i=1}^{N} MI_i\left(\vec{d}(x,y)\right) \tag{10}$$

where MI_i is the MI of the *i*th channel of the start image undergoing the deformation $\vec{d}(x,y)$ and the end image.

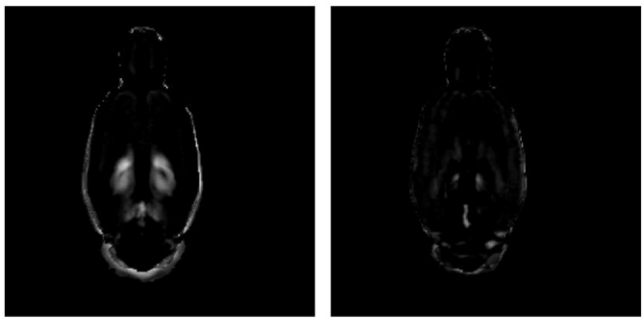

Fig. 4. The difference from the ground truth. Panel A shows the difference of LI method's result from the ground truth, while Panel B shows that of the RI method (using the MI registration method with multi-channels of all DWI). Both images are equally rescaled for better visibility.

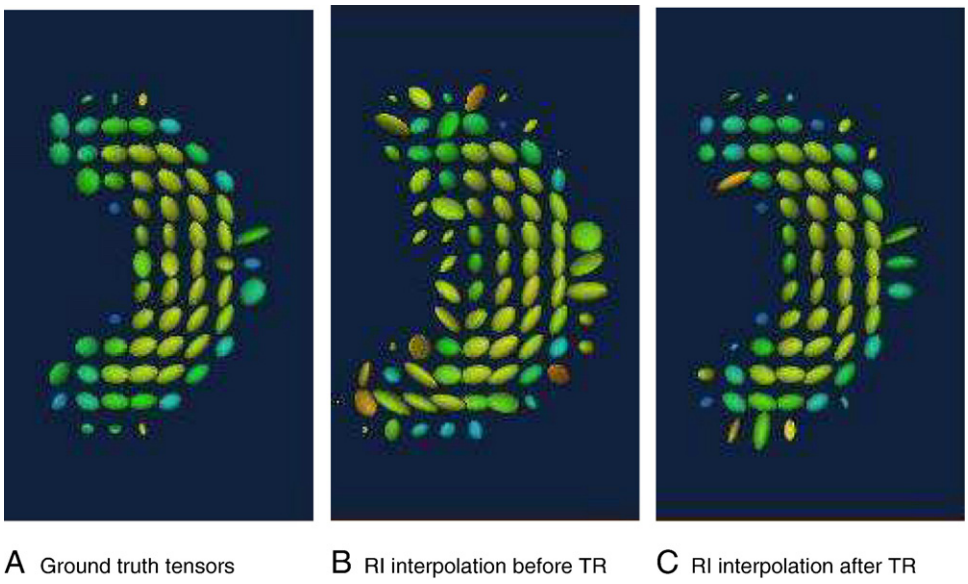

Fig. 5. Panel A shows the ellipsoid representation of the ground truth tensor of the phantom image we used (tensors are color-coded with FA), Panel B shows the INT tensors from our RI method without TR, and Panel C shows the RI method's result after TR.

Different combination are used, including a combination of all DWI (ADW), a combination of DTI (DT) and a combination of all DWI and DTI (DWDT). The choice of ADW is obvious and also in common use, while the use of DT and DWDT are reported to have better results, see [9] and [10]. Note that the MC approach is not applied to the Optical Flow registration. The reason is out of optimization consideration: The scalar components for different channels can vary greatly in magnitude, which, in a multi-channel Optical Flow registration, can result in a lack of sufficient driving force from channels of small scalar magnitude. Consequently, the gradient descent search would be suboptimal. On the other hand, in the MI registration method, the MI similarity measure ensures that driving forces from different channels are comparable in magnitude.

2.2. Interpolation

2.2.1. Modified Registration guided Interpolation

Our interpolation scheme is based on the standard procedure as described in [20]. However, our modified interpolation scheme improves upon it in two ways:

1. Balanced bi-mapping interpolation: Registration-based interpolation methods rely on two assumptions [21]: First, the pair of slices to be registered shares similar anatomical features. Second, the registration algorithm used is able to produce the necessary spatial transformations to map the correspondence from the similar features. While the second assumption can be largely upheld with the sophisticated non-rigid transformation driven by either optical flow or MI, along with the use of a highly dense control grid, the first one is more problematic. Anisotropic real images are often accompanied with large inter-slice changes, e.g., anatomical structures missing from one slice to the next. Therefore, the continuous mapping produced from our smooth-field registration will be unable to characterize this kind of morphology. It is common practice that one performs two registrations on the same pair of slices with different registration directions: first from the start image to the end image, then from the end image to the start image. The final interpolation will be a weighted sum of the two resulting INT images [21]. However, neither the Optical Flow registration nor the MI registration can guarantee a bi-directional mapping, i.e., a mapping, obtained from a start-to-end registration, that is also the result of an end-to-start registration. Consequently, the weighted sum may also result in similar artifacts as in scene-based interpolation. In order to reduce interpolation error in this regard, we

Table 2
A comparison of the DWDI interpolation methods and DiDT interpolation methods with regards to different MSE measures of INT DTI

	MSE_{TC}	MSE_{A}	OVL	MSE_{FA}
LI	$3.35\times.10^{-9}$	0.3550	0.851	$7.57\times.10^{-5}$
wSinc	95.82%	0.3401	0.873	92.21%
EI	100.3%	0.3789	0.842	102.9%
RieI	98.51%	0.3692	0.847	100.3%
OF	92.54%	0.3405	0.890	89.56%
OF+TR	88.96%	0.3225	0.902	89.56%
DWDT	90.45%	0.3395	0.893	87.85%
DWDT+TR	84.78%	0.3165	0.911	87.85%

RI method is shown with and without TR. Only results from real data are shown. Only the actual MSE_{TC} and MSE_{FA} for LI are shown here, the rest of the corresponding entries for other methods in the table are the ratios of their MSE_{TC}/(MSE_{FA}) to LI MSE_{TC}/(MSE_{FA}). The ratio is computed as MSE^{X}_{M}/$MSE^{LI}_{M}\times100\%$, where X stands for one of the methods listed in the table except LI, and M stands for either TC or FA.

introduce a balanced bi-mapping mechanism into the registration. This mechanism is essentially a variant of the multi-channel approach, as it puts the forward (start to end) and backward (end to start) slice pairs in two different channels and minimizes the CEF against two sets of control point displacement vectors $\overrightarrow{d_\phi}$ that are inverse to each other, see Fig. 2.

2. Displacement vectors interpolation: In [20], only one displacement vector was used to evaluate the INT intensity. This is largely justifiable, given a slow-changing displacement field. However, in case of a displacement field with drastic local deformations, one single displacement vector is not enough to reflect the true morphology in the local area. For an example, see Fig. 3. Therefore, for each point (x,y) to be INT, we search four displacement vectors $(\overrightarrow{V_1}, \overrightarrow{V_2}, \overrightarrow{V_3}, \overrightarrow{V_4})$ that bound up this point, and that are closest to it, with the distances to (x,y) as (l_1, l_2, l_3, l_4).

Then, a displacement vector $\overrightarrow{V}$ is INT from these four as:

$$\overrightarrow{V} = \frac{\sum_{i=1}^{4} \frac{\overrightarrow{V_i}}{l_i}}{\sum_{i=1}^{4} \frac{1}{l_i}} \tag{11}$$

$\overrightarrow{V}$ will be used to evaluate the intensity. In general, the bounding vectors can be found within a certain radius

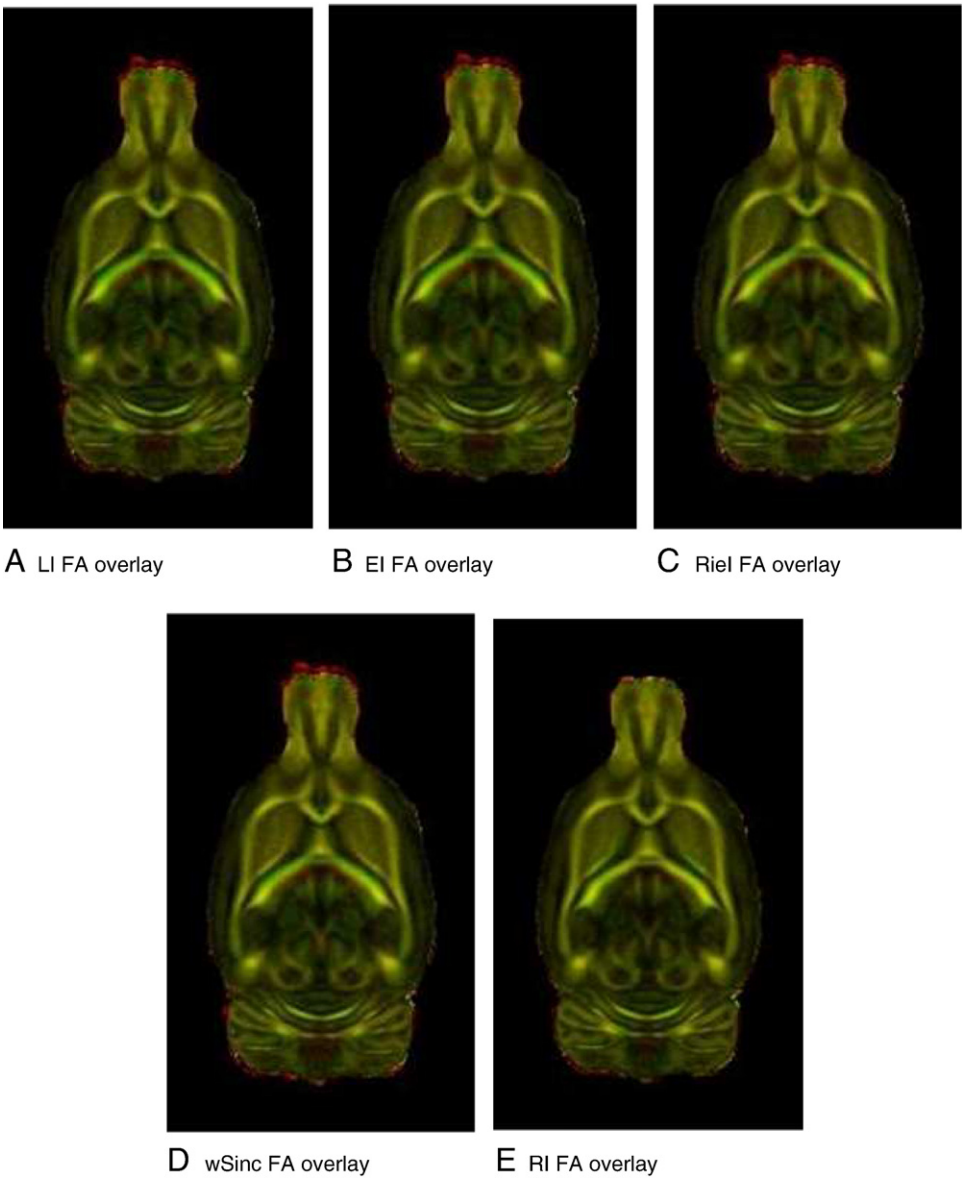

Fig. 6. The FA overlay map. In each figure, the FA of the INT image is given a color code of red, and the FA of the ground truth is given green, and the two images are overlaid. The overlay map will show a color code of yellow where interpolation matches with the ground truth, and either red or green when not matching. One can observe that the RI's overlay map shows less green or red than all the other maps, indicating a higher degree of agreement with ground truth.

of the INT point. Yet, special cases include, for example, that one of the vectors is incident on the point, or that the point is on image boundary so that it does not have four bounding vectors. For the former case, simply the incident vector is used; and for the latter case, the closest vector will be used instead of the interpolation of four bounding vectors.

2.2.2. Tensor reorientation

The registration-based interpolation scheme is designed to achieve optimal DWI interpolation results. However, due to the limitation mentioned in the previous section, one must use the weighted sum of two interpolations obtained from two registrations in opposite directions. This could cause the tensors further estimated from the INT DWI to be not properly oriented, especially not in consistency with its corresponding starting and end tensors on the start and the end slice, respectively. Hence, the need to reorient the INT tensor. TR has been discussed extensively for normal DWI/DTI registration [8,10,22]. The technique we used in this paper is an adaptation of the technique of preservation of principal directions (PPD) [8]. First, for each INT tensor, its corresponding starting tensor and end tensor are found via the incident points of the displacement vector $\overrightarrow{V}$ with which the image intensity is INT. Then, we apply the Jacobian of the local deformation field for interpolation to the start tensor to ascertain the proper orientation of the tensor, i.e., the new eigenvectors $\{\overrightarrow{e_1^i}|i=1,2,3\}$. If the angle between the first eigenvector of the original INT tensor and $\overrightarrow{e_1^i}$ is larger than a threshold angle θ_T, the INT tensor is reoriented according to the new eigenvectors, similar to [8]. The difference of our PPD technique from [8] is that the Jacobian for our local deformation field is 2–dimensional. In order to apply the

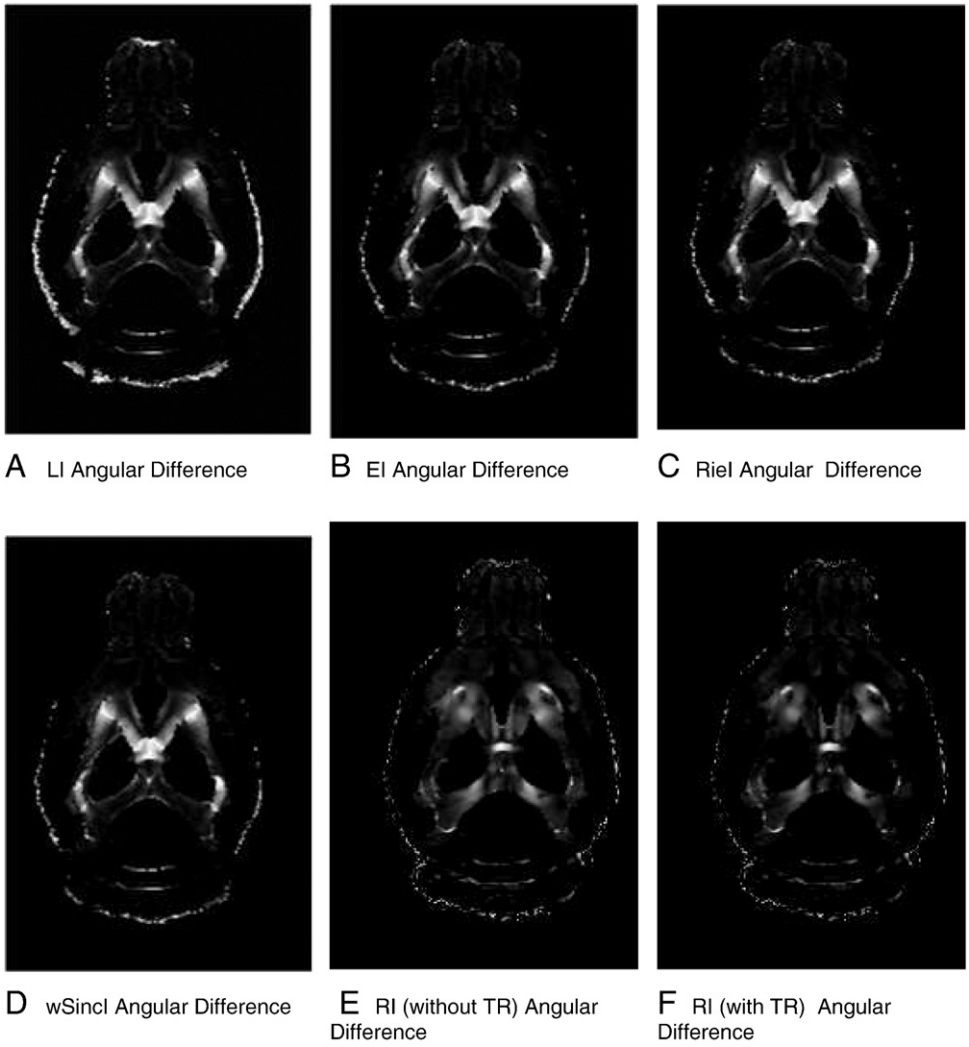

Fig. 7. The angular difference from the ground truth. Panel A shows the angular difference between the first eigenvectors of LI method's result and the ground truth, as computed by arcos ($\overrightarrow{e_1}^{LI}\cdot\overrightarrow{e_1}^{GT}$), scaled between 0°(*black*) and 90°(*white*), and masked with an FA threshold to exclude areas with FA smaller than 0.2. Panel B–D show the angular difference for EI, RieI and wSincI methods. Panel E and Panel F show the angular difference for results from RI without TR and RI with TR, respectively. It can be seen that the RI methods produce significantly less error, and the extra TR step can also further reduce the error.

2D Jacobian to the 3D tensor to reorient it, we construct the 3D Jacobian as

$$\mathbf{J}^{(3)} = \begin{vmatrix} \frac{dx}{dx'} & \frac{dx}{dy'} & 0 \\ \frac{dy}{dx'} & \frac{dy}{dy'} & 0 \\ 0 & 0 & 1 \end{vmatrix} \tag{12}$$

where (x',y') and (x,y) are the coordinate systems for the starting slice and the end slice, respectively, dx/dx' describes the small transformational variation in x caused by a small variation in x', and the other derivatives are similarly interpreted.

3. Experiments and results

In this section, we report the results of our interpolation framework on both phantom and real images. Furthermore, as stated in Section 1, a comparison between the DWDT interpolation and the DiDT interpolation will also be forwarded. The DWDT interpolation methods include linear interpolation (LI), windowed sinc interpolation (wSinc, with a window width=2 [23]), and also our registration-based interpolation (RI); the DiDT interpolation methods include the Euclidean interpolation (EI) and the Riemannian interpolation (RieI). For comparing the DWI interpolation, the conventional mean squared error (MSE) of the INT image with respect to the ground truth image is used. Furthermore, when it comes to the comparison of DTI interpolation, to account for tensor orientations, we use four measures:

1. Tensor Component MSE: It measures the mean squared errors of INT tensor components from the ground truth (GT), and is expressed as follows:

$$MSE_{TC} = \frac{1}{6N}\sum_{n=1}^{N}\sum_{i=1}^{6}\left(\mathrm{DT}_{\mathrm{n,i}}^{\mathrm{INT}} - \mathrm{DT}_{\mathrm{n,i}}^{\mathrm{GT}}\right)^2 \tag{13}$$

where $DT_{n,i}$ is the i^{th} component of the n^{th} tensor, and N is the number of INT tensors.

2. Angular MSE of first Eigenvector: It measures how well the first eigenvector of the INT tensor is aligned to that of the GT, and takes the form:

$$MSE_A = \frac{1}{N}\sum_{n=1}^{N}\arccos\left(\overrightarrow{e}_{n,1}^{INT}\cdot\overrightarrow{e}_{n,1}^{GT}\right) \tag{14}$$

where $\overrightarrow{e}_{n,1}$ denotes the first eigenvector of the n^{th} tensor.

3. Overlapping of Eigenvalue/Eigenvector pair: It measures the overlapping of the INT tensor and the GT tensor. The value 0 indicates zero overlapping, while the value 1 means complete overlapping of the two.

$$OVL = \frac{1}{N}\sum_{n=1}^{N}\frac{\sum_{k=1}^{3}\lambda_{n,k}^{INT}\lambda_{n,k}^{GT}\left(\overrightarrow{e}_{n,k}^{INT}\cdot\overrightarrow{e}_{n,k}^{GT}\right)}{\sum_{k=1}^{3}\lambda_{n,k}^{INT}\lambda_{n,k}^{GT}} \tag{15}$$

where $\lambda_{n,k}$ is the k^{th} Eigenvalue of the n^{th} tensor.

4. Fractional anisotropy (FA) MSE: It measures the mean squared errors between the FA of INT tensor and that of the GT, with the form:

$$MSE_{FA} = \frac{1}{N}\sum_{n=1}^{N}\left(f_n^{GT} - f_n^{INT}\right)^2 \tag{16}$$

where f_n is the FA value for the n^{th} tensor.

We first tested our interpolation framework on the helix phantom generated with the National Alliance for Medical Imaging Computing [24] library. The phantom itself is a helix, with the DT oriented also along the helix. The original image has a dimension of 80×80×20, with one baseline image and 12 DWI for 12 gradient directions. The ground truth for the phantom images can be easily generated by using the same geometrical parameters except doubling the slice number. For real image tests, DWI data sets of rat brain with the dimension of 256×256×29 were used, each with a voxel dimension of 0.137×0.137×0.43 mm^3, and with one baseline image, 6 gradient directions, each direction with 7 repetitions, and in total 42 diffusion weighted images. The ground truth for real data was obtained by extracting slices with the even number indexes, and the interpolation was performed on the remaining odd number slices.

A comparison between the image intensity MSE of the INT helix and the real DWI for LI method, wSinc method and the single/multi channel Optical Flow/MI methods is listed in Table 1 (where the unit for diffusion coefficient is mm^2/s). In general, the object-based methods perform better than the scene-based methods in terms of the MSE of the INT images. This can also be confirmed from the comparison of the difference between LI method and RI in Fig. 4, where the result from RI method is shown to better capture the shape of the image structure. In addition, the MI method is able to achieve more accurate results with a multi-channel approach, and although not all combinations of multi-channel modes serve to better the performance (e.g., the DT case, which lends weight to the argument that the inclusion of DT information is complementary, not essential, to DWI registration), clearly the registration, and consequently the interpolation, benefits from the expansion of information channels.

Now we proceed to demonstrate our results on DTI interpolation. First, we studied the effect of TR on the interpolation, as shown in the phantom example in Fig. 5. Clearly without TR, the tensors can still be misaligned with

respect to the ground truth. The results before and after TR for the three proposed measures along with FA measures are presented in Table 2. First, it can be noticed that, with respect to all error measurements except for the MSE_{TC} measure, DWDT methods in general perform better than DiDT methods. This is not surprising, as a direct interpolation on DTI is more susceptible to the influence of noise or partial volume effect, and as a result the sensitive orientation information can be lost. This gives support to the suggestion that DWDT interpolation is able to produce more accurate results than DiDT interpolation. Moreover, it can also be seen that registration-based methods show significant gains over scene-based methods, regardless of whether those measures are invariant under TR or not. One way to visually demonstrate how well the interpolation matches with the ground truth is an FA overlay map, as shown in Fig. 6, where one can see that the RI result indeed shows less mismatching. Moreover, it is shown that, after TR, the INT tensors are not only in better agreement with the ground truth, with respect to the MSE_{TC} and MSE_{FA} measurements, but also in better angular alignment with it, as is revealed by the angular measurements MSE_A and Overlapping of Eigenvalue/Eigenvector pairs. A comparison of the angular difference in Fig. 7 also confirms it.

4. Conclusion

In this work, we have established an up-sampling framework specifically for DWI/DTI. The framework is able to extract the underlying feature information via a non-rigid registration to guide the interpolation. Furthermore, compared to other scene-based interpolation methods such as linear interpolation or the higher order windowed sinc interpolation, it is also able to achieve a better interpolation. Moreover, it is also demonstrated that, when processing real data, an extra Tensor Reorientation step is helpful in bringing the INT DT to a better agreement with the ground truth. Furthermore, a comparison between two method groups for DTI interpolation also suggests that up-sampled DTI, estimated from up-sampled DWI, are able to approximate the ground truth better than up-sampled DTI that are directly INT from the low-resolution DTI.

For future investigations, it would be interesting to fully exploit the influence of extra channel of image information (FA, mean diffusivity, etc.) on the registration and ultimately the interpolation, also would be of interest to quantify, locally and with robust statistics, the influence of registration on the interpolation as well as the tensor reorientation. Furthermore, the registration-guided interpolation process itself can be regarded as a constraint variational problem, from which the interpolation is obtained as a minimizer of certain functional under various constraints. Therefore, it would be beneficial to broaden the framework onto this mathematical background, and to fully investigate the possibilities of different constraints and solution methods.

Acknowledgment

The work presented in this paper was partly supported by the IWT SBO grant 060819 "*Quantivium*". The authors also wish to thank Jelle Veraart and Steve De Backer for their useful discussions.

Appendix A. Supplementary data

Supplementary data associated with this article can be found, in the online version, at doi:10.1016/j.mri.2010.06.018.

References

[1] Udupa JK, Herman GT. 3D imaging in medicine. Boca Baton, Florida: CRC Press, Inc.,; 1991.
[2] Grevera GJ, Udupa JK. An objective comparison of 3-d image interpolation methods. IEEE Trans Med Imaging 1998;17(4):642–52.
[3] Meijering EHW, Niessen WJ, Viergever MA. Quantitative evaluation of convolution-based methods for medical image interpolation. Med Image Anal 2001;5(2):111–26.
[4] Thévenaz P, Blu T, Unser M. Interpolation revisited. IEEE Trans Med Imaging 2000;19(7):739–58.
[5] Goshtasby A, Turner DA, Ackerman V. Matching of tomographic slices for interpolation. IEEE Trans Med Imaging 1992;11(4):507–16.
[6] ITK. Insight Toolkit. www.itk.org, 2009.
[7] Tschumperle D, Deriche R. Diffusion PDE's on vector-valued images: local approach and geometric viewpoint. IEEE Signal Process Mag 2002;19(5):16–25.
[8] Alexander DC, Gee JC, Bajcsy R. Strategies for data reorientation during non-rigid warps of diffusion tensor images. Lect Notes Comput Sci 1999;1679:463–72.
[9] Rohde GK, Pajevic S, Pierpaoli C. Multi-channel registration of diffusion tensor images using directional information. In IEEE International Symposium on Biomedical Imaging; 2004. p. 712–5.
[10] Van Hecke W, Leemans A, d' Agostino E, De Backer S, Vandervliet E, Parizel P, et al. Nonrigid coregistration of diffusion tensor images using a viscous fluid model and mutual information. IEEE Trans Med Imaging 2007;26(11):1598–612.
[11] Studholme C. Dense feature deformation morphometry: incorporating DTI data into conventional MRI morphometry. Med Image Anal 2008;12(6):742–51.
[12] Chao TC, Chou MC, Yang P, Chung HW, Wu MT. Effects of interpolation methods in spatial normalization of diffusion tensor imaging data on group comparison of fractional anisotropy. Magn Reson Imaging Jun 2009;27(5):681–90.
[13] Pennec X, Fillard P, Ayache N. A Riemannian framework for tensor computing. In Int J Comput Vision 2006;66(1):41–66.
[14] Beauchemin SS, Barron JL. The computation of optical flow. ACM New York; 1995.
[15] Tekalp AM. Digital Video Processing. Prentice-Hall; 1995.
[16] Lee S, Wolberg G, Chwa KY, Shin SY. Image metamorphosis with scattered feature constraints. In IEEE Transactions on Visualization and Computer Graphics, Vol. 2; 1996. p. 337–45. No. 4.
[17] Lee S, Wolberg G, Shin SY. Scattered data interpolation with multilevel B-splines. In IEEE Transactions on Visualization and Computer Graphics, Vol. 3; 1997. p. 228–44. No. 3.
[18] Lucas B, Kanade T. An iterative image registration technique with an application in stereo vision. In Seventh International Joint Conference on Artificial Intelligence (IJCAI-81); 1981. p. 674–9.

[19] Park HJ, Kubicki M, Shenton ME, Guimond A, McCarley RW, Maier SE, et al. Spatial normalization of diffusion tensor MRI using multiple channels. Neuroimage 2003;20(4):1995–2009.
[20] Penney GP, Schnabel JA, Rueckert D, Viergever MA. Registration-based interpolation. IEEE Trans Med Imaging 2004;23(7):922–6.
[21] Frakes DH, Dasi LP, Pekkan K, Kitajima HD, Sundareswaran K, Yoganathan AP, et al. A new method for registration-based medical image interpolation. IEEE Trans Med Imaging 2008;27(3):370–7.
[22] Cao Y, Miller MI, Winslow RL, Younes L. Large deformation diffeomorphic metric mapping of vector fields. IEEE Trans Med Imaging 2005;24(9):1216–30.
[23] Meijering EHW, Niessen WJ, Josien P, Viergever MA. Quantitative Comparison of sinc-approximating kernels for medical image interpolation. In MICCAI; 1997. p. 210–7.
[24] NA-MIC. The National Alliance for Medical Imaging Computing; 2006. www.na-mic.org.